In Situ Amplification of Intracellular MicroRNA with MNAzyme Nanodevices for Multiplexed Imaging, Logic Operation, and Controlled Drug Release

Penghui Zhang,[†] Zhimei He,[†] Chen Wang,[‡] Jiangning Chen,[‡] Jingjing Zhao,[†] Xuena Zhu,[§] Chen-Zhong Li,[§] Qianhao Min,[*,†] and Jun-Jie Zhu[*,†]

[†]State Key Laboratory of Analytical Chemistry for Life Science, School of Chemistry and Chemical Engineering, Nanjing University, Nanjing 210093, People's Republic of China, [‡]State Key Laboratory of Pharmaceutical Biotechnology, Jiangsu Engineering Research Center for microRNA Biology and Biotechnology, School of Life Sciences, Nanjing University, Nanjing 210093, People's Republic of China, and [§]Nanobioengineering/Nanobioelectronics Laboratory, Department of Biomedical Engineering, Florida International University, Miami, Florida 33174, United States

ABSTRACT MicroRNAs (miRNAs), as key regulators in gene expression networks, have participated in many biological processes, including cancer initiation, progression, and metastasis, indicative of potential diagnostic biomarkers and therapeutic targets. To tackle the low abundance of miRNAs in a single cell, we have developed programmable nanodevices with MNAzymes to realize stringent recognition and *in situ* amplification of intracellular miRNAs for multiplexed detection and controlled drug release. As a proof of concept, miR-21 and miR-145, respectively up- and down-expressed in most tumor tissues, were selected as endogenous cancer indicators and therapy triggers to test the efficacy of the photothermal nanodevices. The sequence programmability and specificity of MNAzyme motifs enabled the fluorescent turn-on probes not only to sensitively profile the distributions of miR-21/miR-145 in cell lysates of HeLa, HL-60, and NIH 3T3 (9632/0, 14147/0, 2047/421 copies per cell, respectively) but also to visualize trace amounts of miRNAs in a single cell, allowing logic operation for graded cancer risk assessment and dynamic monitoring of therapy response by confocal microscopy and flow cytometry. Furthermore, through general molecular design, the MNAzyme motifs could serve as three-dimensional gatekeepers to lock the doxorubicin inside the nanocarriers. The drug nanocarriers were exclusively internalized into the target tumor cells *via* aptamer-guided recognition and reopened by the endogenous miRNAs, where the drug release rates could be spatial-temporally controlled by the modulation of miRNA expression. Integrated with miRNA profiling techniques, the designed nanodevices can provide general strategy for disease diagnosis, prognosis, and combination treatment with chemotherapy and gene therapy.

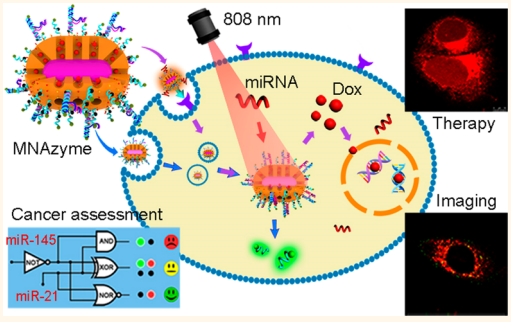

KEYWORDS: DNAzyme · microRNAs · logic operation · intracellular imaging · drug delivery

MicroRNAs (miRNAs) are ~22 nt noncoding RNAs; they are involved in virtually all the cellular processes through imperfect pairing with target mRNAs (mRNAs) and post-transcriptional regulation of their encoded protein expression.[1,2] Especially during the cancer initiation, progression, and metastasis, miRNAs can function either as oncogenes or tumor suppressors, showing as up- or down-regulated expression in the malignant tissues *versus* their normal counterparts.[3] Many reports have proposed that miRNA expression profiling is a powerful tool to depict the clinical characteristics of tumors, including tissue origin, differentiation, aggression, and response to therapy;[4,5] it not only provides promising candidate biomarkers for cancer diagnosis and prognosis, but also screens out potential targets for drug and gene therapy.[6]

Currently, masses of strategies are developed for miRNA profiling in extracted RNA from cell lysate on the basis of Northern blotting, microarray hybridization, and

* Address correspondence to jjzhu@nju.edu.cn, minqianhao@nju.edu.cn.

Received for review November 5, 2014 and accepted December 19, 2014.

Published online December 19, 2014
10.1021/nn506309d

quantitative RT-PCR (qRT-PCR).[7] However, due to their small size, low abundance, and high sequence similarity, intracellular miRNA detection is hampered by the insufficient readout signal from a single bound probe.[8] Although many novel methods derived from fluorescence *in situ* hybridization (FISH) have been developed for single-cell miRNA detection with multiple labeled molecular beacons or enzymes to amplify the output signal, a noninvasive manner for real-time monitoring of the dynamic variation of miRNAs in living cells is urgently needed in clinical research.[9−12] On the other hand, considering the significant difference of miRNA expression levels in different tissues, even in different cancer subtypes,[13] we have exploited the use of miRNA molecules as an endogenous stimulus to realize controlled drug release in tumor cells.[14] Compared with the external stimuli (light, temperature, and magnetic field) and internal triggers (pH, enzymes, molecules, and reducing agents),[15−17] miRNAs not only exhibited considerable expression distinction between tumor and normal tissues but also served as a synergetic therapy target by gene regulation, taking pride in enhanced therapeutic efficacy and minute side effects. Nevertheless, it should be noted that even for the most overexpressed miRNA in tumor cells, its release efficiency was still far from ideal due to the low amounts of miRNAs, which usually varied from a few copies to over 50 000 copies per cell.[18] Thus, whether for intracellular imaging or for controlled drug release, an efficient amplification strategy should be developed to make the most of endogenous miRNAs.

In the analysis of gene targets, highly sensitive and specific detection has been achieved in homogeneous solution by means of enzymatic amplification techniques, such as polymerase chain reaction (PCR), rolling circle amplification (RCA), ligation chain reaction, and isothermal amplification.[19,20] But in intracellular sensing, it is a great challenge to co-deliver the enzymes and their substrates into cells so as to reconstruct the enzymatic amplification reaction *in situ*. Deoxyribozymes (DNAzymes) are single-strand nucleic acids that can catalyze some chemical reactions, among which the RNA/DNA cleavage and peroxidase-mimicking catalytic activity are extensively used to amplify signals in DNA, protein, and metal ion sensors.[21−24] In particular, through molecular design, DNAzymes can be easily coupled with their oligonucleotide substrates and specific DNA sequences to synthesize multifunctional DNA hybrids, which are able to specifically recognize target miRNAs by complementary base paring or interact with target cells by aptamer-guided binding, providing possibilities for stringent recognition and *in situ* signal amplification in tumor cells simultaneously.

In this study, we have split DNAzymes into multicomponent nucleic acid enzymes (MNAzymes) and assembled them on the surface of mesoporous silica-coated gold nanorods (MSGRs) to construct

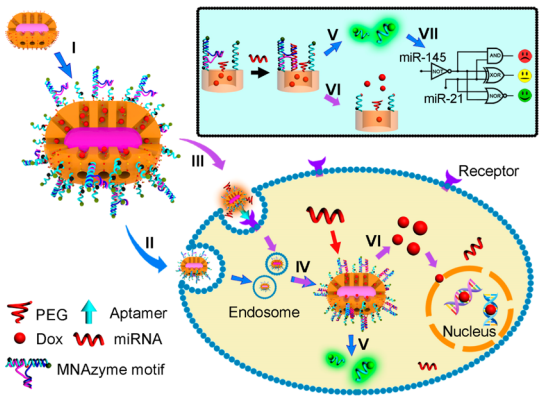

Figure 1. Schematic illustration of the MNAzyme-based nanodevices for miRNA intracellular imaging and controlled drug release. Inset is the mechanism of the MNAzyme-mediated amplification strategy for miRNA detection and controlled drug release. I, preparation of MMSGR nanodevices; II, clathrin-mediated endocytosis of MMSGR probes; III, receptor-mediated endocytosis *via* aptamer; IV, endosome escape; V, intracellular miRNA imaging; VI, miRNA-triggered Dox release; VII, logic operation for cancer risk assessment.

multifunctional nanodevices for intracellular miRNA imaging and controlled drug release. As shown in Figure 1, two parts of the MNAzyme formed an inactive DNA motif with their substrate through partial paring at the end of each strand, where the cleavage was blocked due to conformation mismatch. In the presence of target miRNAs, the conformation of MNAzymes was rearranged to activate their catalytic ability, resulting in the cleavage of the fluorescently labeled substrate strands; the active MNAzymes would autonomously move to the neighboring substrates for further cleavage, thus generating an enzymatically amplified fluorescence signal. The embedded gold nanorods functioned as temperature controller by converting the near-infrared (NIR) light into heat, making it possible to optimize enzymatic efficiency of MNAzyme-modified MSGRs (MMSGRs) by finely tuning successive NIR irradiation *in vivo*.[25] Furthermore, by convenient sequence adjustment, two MMSGR probes, responsive to miR-21 and miR-145, which were respectively up- and down-regulated in most tumor cells, were designed to fabricate a logic gate to assess the degree of cancer risk. On the other hand, with further drug loading, PEGylation, and aptamer conjugation, multifunctional nanocarriers were constructed with the MNAzyme motifs as gatekeepers to block the doxorubicin (Dox) inside the pores. Once exclusively internalized into the target tumor cells by aptamer recognition, the intracellular miRNAs served as a specific key to initiate the MNAzyme-catalyzed cleavage of substrates, inducing gradual dissociation of the MNAzyme motifs from the mesopores and thereby triggering controlled drug release.

RESULTS AND DISCUSSION

Preparation and Characterization of MNAzyme-Modified Nanodevices. The mesoporous silica-coated gold nanorods

modified with chloro and amine groups were prepared according to a base-catalyzed sol−gel procedure with gold nanorods (GRs) as seeds. The MSGRs had a uniform size of 80−100 nm in diameter and MCM-41 hexagonal structures (Supporting Information Figures S1 and S2), and their pore size, surface area, and average pore volume were estimated to be 3.3 nm, 205.2 m^2 g^{-1}, and 0.286 cm^3 g^{-1} from the nitrogen adsorption−desorption data (Supporting Information Figure S3). The chloro groups on the surfaces of MSGRs were substituted with azide groups, which subsequently coupled with hexynyl-modified substrate DNA (sub-DNA) *via* copper(I)-catalyzed azide−alkyne cycloaddition at 4 °C to obtain sub-MSGRs.[26] Then the MNAzyme sequences hybridized with their substrates on the sub-MSGRs' surface to yield a triplex MNAzyme motif, which could lock the mesopores like a gatekeeper in an inactive conformation, while cleaving the substrate like a scissor in the active conformation. The surface functionalization processes were confirmed in Supporting Information Figures S4 to S7, in which an increased hydrodynamic diameter of 139 ± 11 nm and reversed zeta potential of −22.3 ± 1.6 mV verified the successful conjugation of the MNAzyme motif onto MSGRs. The densities of the anchored sub-DNA and MNAzyme motif on MMSGRs were quantitatively optimized to be 484 and 205 nmol $nmol^{-1}$ for further miRNA detection and drug entrapment. Meanwhile, the efficiency of photothermal conversion was investigated as shown in Supporting Information Figure S8. In this case, the nanoparticles could rapidly heat the surrounding medium upon a gentle NIR irradiation, which was favorable in maximizing the cleavage activity of the MNAzymes and minimizing side effects *in vitro* or *in vivo*.

Detection of miRNAs by MMSGR Probes. Figure 2a depicts the mechanism of the miR-21-triggered and MNAzyme-mediated signal amplification. The MNAzyme exists in partzymes A and B, each of which contains a target-binding sensor arm, partial catalytic core, and probe-binding substrate arm. The substrates labeled with a fluorophore and a quencher on each side of the cleavage site assembled with A and B to form a stable inactive MNAzyme motif, which was confirmed by the single emission band in lane 1 (Figure 2b). The addition of target miRNA reconstructed the MNAzyme motif and activated its cleavage function, resulting in the rupture of the substrate and recovery of the fluorescence. Then the active MNAzymes were recycled to digest multiple substrates, concomitantly generating continuous fluorescence increase. Consequently, small amounts of miRNAs completely cleaved 100-fold substrates in 1.5 h (lane 2 in Figure 2b), providing a rapid path for the amplified detection of miRNAs. The function of the MNAzyme motif assembled on MMSGRs was corroborated in Figure 2c, in which the probes displayed rapid response to miR-21 in a concentration-dependent

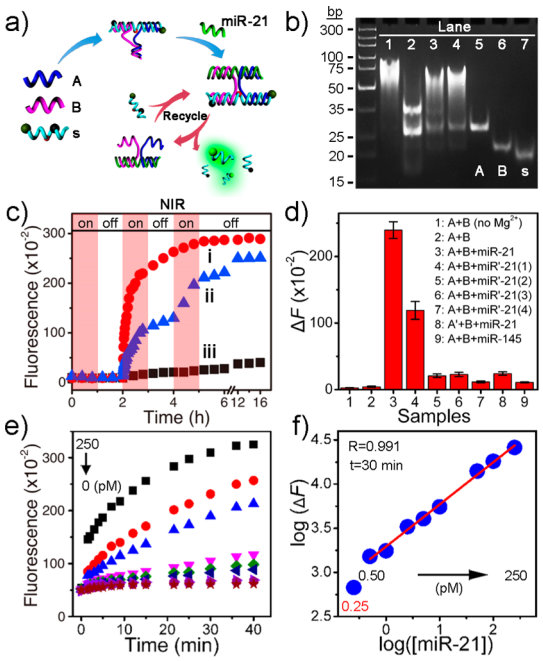

Figure 2. Detection of miRNAs with MMSGRs probes. (a) Mechanism of the MNAzyme-mediated amplification strategy in detecting miRNAs. A, partzyme A; B, partzyme B; s, substrate. (b) Determination of the MNAzyme cleavage activity by polyacrylamide gel electrophoresis. The samples (1) A+B+s and (2−4) A+B+s+miR-21 were incubated at 50 °C for 1.5 h (lanes 1, 2), 1 h (lane 3), and 0.5 h (lane 4). (c) Time-dependent fluorescence variations of 10 pM MMSGRs probes in Tris-HCl containing 5 mM Mg^{2+} with the addition (i) 250 pM miR-21, (ii) 10 pM miR-21, and (iii) 250 pM miR-145 at 2 h. (d) Investigation of the specificity of the MMSGR probes upon the treatment with different control miRNAs for 1 h. Error bars indicate SD (n = 3). (e) Time-dependent fluorescence changes of 10 pM probe-21 upon the addition of miR-21 with different concentrations. (f) Relationship between the fluorescence change and the miR-21 concentration at 30 min.

manner, especially upon NIR irradiation. Meanwhile, the temperature-dependent characteristic of MNAzymes was investigated in Supporting Information Figure S9, which showed that MMSGRs achieved an optimal cleavage at 45 °C or under NIR exposure with a power density of 2 W cm^{-2}, indicating the efficient photothermal conversion of the gold nanorods. In contrast, the fluorescence exhibited a minute change upon the addition of miR-145, which suggested that MMSGRs had an excellent stability and selectivity.

A series of control experiments were performed to further prove the high specificity and discrimination of MMSGRs to miR-21 mimics with one- or two-base mismatch. The fluorescence variations in Figure 2d suggested that the perfect hybridization of the MMSGRs with their target miR-21 could efficiently initiate the cleavage reaction, whereas the mismatch in the middle of the miRNAs (groups 5, 6, 7) would drastically reduce the enzyme activity. Thus, only the stringent target hybridization with a larger thermodynamic energy change could open the triplex loop of the MNAzyme motif and switch it to active form. So even if the

mismatched base was located at the terminus (group 4), a discrimination factor of 2.3 was still obtained, implying the high selectivity of our probes in distinguishing an miRNA family with high sequence homology.

Finally, the sensitivity of the MMSGRs was determined by monitoring the fluorescence changes of 10 pM MMSGRs upon the treatment with different concentrations of miR-21. The curves in Figure 2e showed that the probes had a rapid response to 250 pM miR-21 and then leveled off to a saturation value in a short time, but showed a continuous cleavage at a declining rate with the decrease of concentration. Furthermore, by recording the fluorescence change at 30 min, a calibration curve was fitted with a linear range from 0.5 to 250 pM and a detection limit of 0.25 pM. The high selectivity and sensitivity make it possible to apply the probes in detecting the trace amounts of miRNAs in cancer cells.

Construction of a Logic Gate by MMSGR Probes for Cancer Risk Assessment. As the most potential marker for cancer diagnosis, miR-21, one kind of oncogene, is significantly overexpressed in a wide variety of cancers, including glioblastoma, breast, lung, pancreas, liver, cervical, and various hematopoietic cancers; it acts as an inhibitor in cell apoptosis and as a promoter in tumor invasion and metastasis.[27] However, false positive results would be obtained if we take miR-21 as the only detection index because other diseases such as cardiovascular disease might also induce aberrant expression of miR-21.[28] As a proof of concept, we selected miR-145 to construct a logic gate with miR-21 for assessing cancer risk; miR-145 acts as a tumor suppressor with antiproliferative function, showing a down-regulated expression in many cancers.[29,30] First, by flexibly adjusting the sequences of the sensor arms and substrate arms of the MNAzymes, probe-21 and probe-145 labeled with organic dyes FAM and TAMRA were designed for the detection of miR-21 and miR-145, respectively. Similar to probe-21, probe-145 showed a sensitive and specific response to miR-145 with a linear range between 2.5 and 250 pM and a detection limit of 1.0 pM in Supporting Information Figure S10. As expected in Figure 3a–d, the mixed probes were treated with equivalent miR-21 and miR-145 under NIR light with an optimized power density of 2 W cm^{-2} (Supporting Information Figure S11), resulting in the cleavage of respective probes and the output of two independent fluorescence signals without cross-reactivity. In consideration of different expression levels of miRNAs between cancer tissues and normal tissues, as a proof of concept, we have chosen HeLa as control cells and estimated the amounts of miR-21 and miR-145 in 10^6 cells according to the PCR results in Figure 3d and the published abundance of miR-21 (~20 000 copies per cell).[31] On the basis of the above estimated concentration, the fluorescence intensities respectively corresponding to 10 pM miR-21 and 1 pM miR-145 were set as the threshold values for logic operation, while the fluorescence above the threshold meant input "1". Accordingly, an OR gate (G1) was constructed in Figure 3e with 50 pM miR-21 and miR-145 as inputs for the activation of a logic gate operation and dual fluorescence signals as outputs to assess the cancer risk of the patients. Before the OR logic operation, a NOT gate was implemented in advance so as to invert the down-regulation of miR-145 (input "0") to the input "1" of the OR gate as illustrated in Figure 3f. The operation results revealed that aberrant expression of any miRNAs would lead to a true output "1", indicating a high cancer risk, while the output "0" suggested the risk of patients having cancer was low. However, the G1 device could not discriminate the miRNA dysregulation caused by other diseases or environmental changes, resulting in serious false positives.

For a more accurate cancer risk rating, a modified half adder device (G2) that produced Sum and Carry outputs was designed that required the implementation of the AND, XOR, and NOR gates in a single test. The fluorescence signals corresponding to the outputs of the three gates are presented in Figure 3e, where the Carry bit (AND gate) giving a green fluorescence with inputs (1,0) is classified as Red Alert, indicating an ultrahigh risk in cancer. The Sum bits give "True" output if only one of miR-21 and miR-145 is aberrantly expressed, which are classified as Yellow Alert, indicating a high risk of cancer and a urgent need for further screening tests, while the NOR gate outputs a red fluorescence as "True" with a classification of Green Alert, meaning a low danger of cancer. The validity of the G2 logic device was confirmed by detecting the practical samples of cell lysates from 10^6 HeLa, NIH 3T3, and HL-60 cells. As shown in the inset images of Figure 3b and c, the output fluorescence signals could be directly used to perform the logic operation, which revealed that HeLa and HL-60 cancer cells were rated as Red Alert while NIH 3T3 as Green Alert. The operation outputs were consistent with the PCR results in Figure 3d, indicating the high efficacy of the logic device in cancer risk assessment. Additionally, miR-143, another tumor suppressor down-expressed in tumor tissues, can be employed in the same fashion as the third input to construct a multiple logic device for more accurate assessment.[30] More notably, by virtue of the high sensitivity of the nanoprobes, the concentrations of miR-21 in each cell samples were calculated from the calibration curves as 32 pM (HeLa), 6.8 pM (NIH 3T3), and 47 pM (HL-60) with estimated distributions of 9632, 2047, and 14 147 copies per cell, respectively. Otherwise, no detectable signals of miR-145 were observed in HeLa and HL-60, whereas it exhibited a high content of 1.4 pM in NIH 3T3 (421 copies per cell).

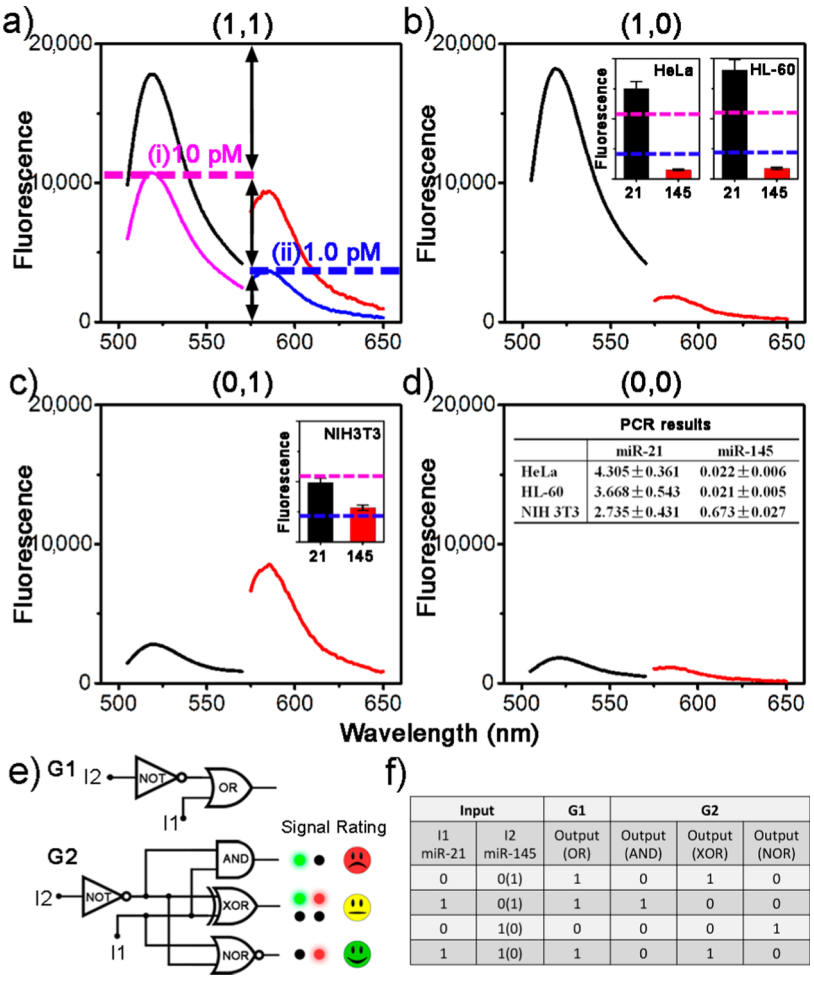

Input		G1	G2		
I1 miR-21	I2 miR-145	Output (OR)	Output (AND)	Output (XOR)	Output (NOR)
0	0(1)	1	0	1	0
1	0(1)	1	1	0	0
0	1(0)	0	0	0	1
1	1(0)	1	0	1	0

	miR-21	miR-145
HeLa	4.305±0.361	0.022±0.006
HL-60	3.668±0.543	0.021±0.005
NIH 3T3	2.735±0.431	0.673±0.027

Figure 3. Construction of logic devices with MMSGR probes for cancer risk assessment. Dual fluorescence outputs of 10 pM probe-21 and probe-145 with the addition of 50 pM miR-21 (I1) and miR-145 (I2) as inputs: (a) both inputs I1 and I2 (1,1), (b) input I1 (1,0), (c) input I2 (0,1), and (d) no input (0,0). Inset images in (b) and (c) are the fluorescence intensities of the mixed probes generated by the addition of the cell lysate of HeLa, HL-60, and NIH 3T3 cells. Inset table in (d) is the miRNA profiles detected by qRT-PCR. Error bars indicate SD (n = 3). (e) Logic scheme for the G1 and G2 modules. The color points in Signal: green, probe-21; red, probe-145; dark, no fluorescence. In the rating system for cancer risk assessment, Red Alert signals an ultrahigh risk; Yellow Alert, a high risk; and Green Alert, a low danger of cancer. (f) Truth table of G1 and G2. The NOT gate was performed to invert the down-regulation of miR-145 (input "0"), which usually occurred in cancer cells to the input "1" of the following logic operation.

Intracellular Imaging of miRNAs with MMSGRs Probes. As a fluorescence probe for cancer diagnosis, the MMSGR probe presents a turn-on behavior in response to its target miRNA, which is favorable to visualizing miRNAs *in situ* in a single cell because its low background signal effectively increases the detection sensitivity. Prior to miRNA imaging, the cellular uptake and intracellular trafficking of the probes were explored to make sure that the probes could be efficiently internalized and released into the cytoplasm. The control experiments in Supporting Information Figure S12 demonstrated that the sequence changes of the MNAzyme exerted a minute influence on the uptake amounts of different probes; the negatively charged silica nanoparticles were nonspecifically internalized into the HeLa cells in 6 h *via* a clathrin-mediated mechanism.[32] Due to the substantial decrease of the pH value (from 7.4 in the cytoplasm to ~5.5 in the endosome), the amine groups grafted on the surface of MMSGRs acted as a proton sponge to disrupt the endosome membranes, leading to a rapid escape of the probes into the cytoplasm, where the MNAzyme cleavage was initiated by the endogenous miRNAs.[33] The successful endosome escape was confirmed by the poor correlation of the red and green fluorescence respectively corresponding to endosome/lysosome and cleaved probes in the confocal laser scanning microscope (CLSM) images (Figure 4a).

Next, the expression levels of different miRNAs in HeLa cells were evaluated with probe-21 and probe-145 by CLSM and flow cytometry in Supporting Information Figure S13. Compared with the weak red fluorescence, the strong green one in the CLSM images and the flow cytometric results represented that more labeled substrates on probe-21 were cleaved inside the HeLa cells, reflecting a higher abundance of miR-21

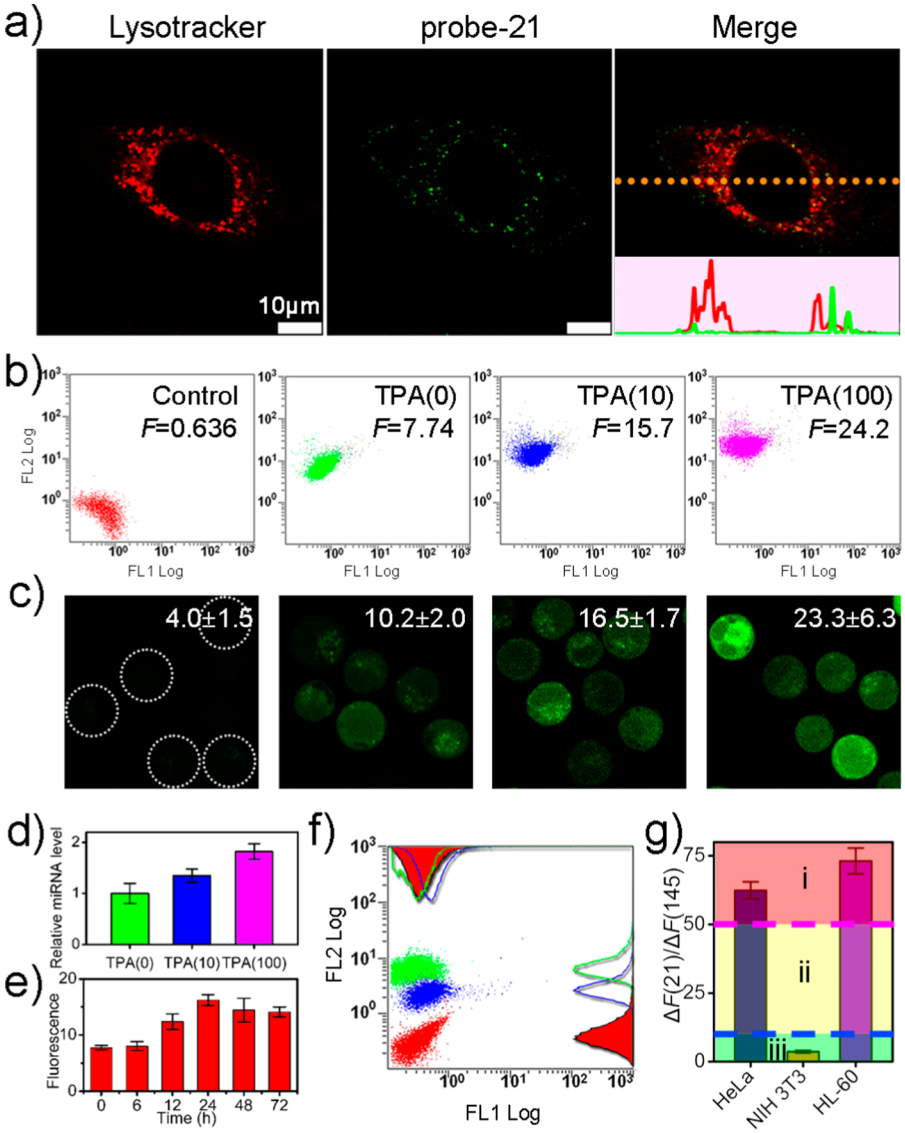

Figure 4. Intracellular imaging of miRNAs with MMSGR probes. (a) CLSM images of the HeLa cells with the treatment of probe-21. Inset is the fluorescence intensity variations along the marked line, while the red color comes from the endosome/lysosome stained by Lysotracker and the green one from the cleaved probes. (b) Evaluation of the miR-21 expression levels with probe-21 by flow cytometric analysis after treating the HL-60 cells with 0, 10, and 100 nM TPA drugs for 24 h. (c) Evaluation of the influence of drug treatment on the expression levels of miR-21 in HL-60 cells by CLSM. (d) miR-21 expression levels of HL-60 cells determined by qRT-PCR after drug treatment. (e) Evaluation of the miR-21 expression variation with the time after the drug treatment. The HL-60 cells were incubated with 10 nM TPA for 24 h and further cultured with fresh medium for a certain time. (f) Simultaneous analysis of miR-21 and miR-145 in HeLa (green) and NIH 3T3 (blue) cells with probe-21 and probe-145 by flow cytometry. The red was the control group. (g) Assessment of the cancer risk with the signal ratio (R) of miR-21 to miR-145 from the flow cytometric results: (i) ultrahigh, $R > 50$; (ii) high, $50 > R > 10$; (iii) low, $R < 10$. All the error bars indicate SD ($n = 3$).

than miR-145. Furthermore, the MMSGR probe was used to assess the expression variation of miR-21 in HL-60 cells treated with 12-*O*-tetradecanoylphorbol-13-acetate (TPA), which could induce differentiation of the cells into monocyte/macrophage-like cells and up-regulation of miR-21.[34] With the increase of TPA concentrations, the fluorescence intensity was observed to be enhanced in both flow cytometric and CLSM results (Figure 4b and c), verifying the up-regulation of miR-21 in TPA-induced cells, which was in agreement with the PCR results in Figure 4d. Meantime, the dynamic changes of miR-21 in TPA-treated cells were monitored by flow cytometry in Figure 4e, demonstrating a maximum fluorescence value after removing the drug medium for 24 h. Finally, equivalent probe-21 and probe-145 were incubated with different cells to measure miR-21 and miR-145 simultaneously. Due to the low abundance of miR-145, it was hard to separate the fluorescence signal of probe-145 from the mixed probes in multichannel confocal images. However, the flow cytometric results in Figure 4f revealed that the HeLa and NIH 3T3 cells could be clearly distinguished into different groups by the fluorescence, indicating the potential of the combined probes in sorting cancer

cells from the normal cells. Additionally, the flow cytometric results also could be used to perform the G2 logic operation or develop a ratio method using fluorescence signals (Figure 4g) to conveniently estimate the cancer risk of the tested samples.

Controlled Dox Release Triggered by Intracellular miRNAs. Besides the recognizing and catalyzing functions encoded in the sequences, the structures of DNA, including C-quadruplex, duplex, and single strand, could be employed as gatekeepers for trapping drugs in the channels of mesoporous silica.[35−38] Thus, we next investigated whether the multifunctional nanodevices could achieve drug delivery and controlled release in target tumor cells with the mesoporous silica shell as the drug container, MNAzyme motif as gatekeeper, and the gold nanorod as heat generator. The general experimental procedure was conducted as stated in the Materials and Methods. The cells were first incubated with the cultured medium containing nanocarriers for 6 h. After the replacement with fresh medium and exposure under NIR light for 30 min, the cells were cultured for a certain time until the CLSM, flow cytometry, or MTT tests were performed. Unlike the similar distributions of MMSGRs-Dox in both cells, aptamer hybridization and PEGylation brought about a preferable accumulation of MMSGRs-Dox-Apt/PEG in HeLa rather than in NIH 3T3 cells (Supporting Information Figure S14) *via* the recognition between the AS1411 aptamer and the nucleolin overexpressed on HeLa surfaces, which was beneficial for alleviating side effects during cancer therapy. Once the nanocarriers with a Dox loading capacity of 68.4 mg g^{-1} were exposed in the cytoplasm, as shown in Figure 5a, the endogenous miRNAs rearranged the MNAzyme motif and triggered the cleavage reaction until all the substrates were cleaved, leading to the dissociation of the MNAzyme motif from the silica surfaces and concomitant drug release. Figure 5b and c demonstrated that even though equivalent amounts of nanocarrier-21 and nanocarrier-145 were internalized, a faster Dox accumulation was observed in the nuclei of HeLa cells treated with nanocarrier-21 at 3 h, consequently resulting in severe cell death with the appearance of massive apoptotic bodies (Figure S15). This difference manifested that the intracellular miRNA-triggered drug release behaved in a concentration-dependent manner, which was consistent with the release profiles in PBS solution in Supporting Information Figure S16. Notably, by virtue of the MNAzyme-mediated amplification, a trace amount of endogenous miRNAs efficiently opened the gatekeeper, and thus even the low-abundant miR-145 could trigger considerable Dox release and induce a continuous mortality of HeLa cells (Supporting Information Figure S17).

Furthermore, we tested the nanocarriers in combination with gene therapy by transfecting miRNA mimics or inhibitors into the HeLa cells. As expected,

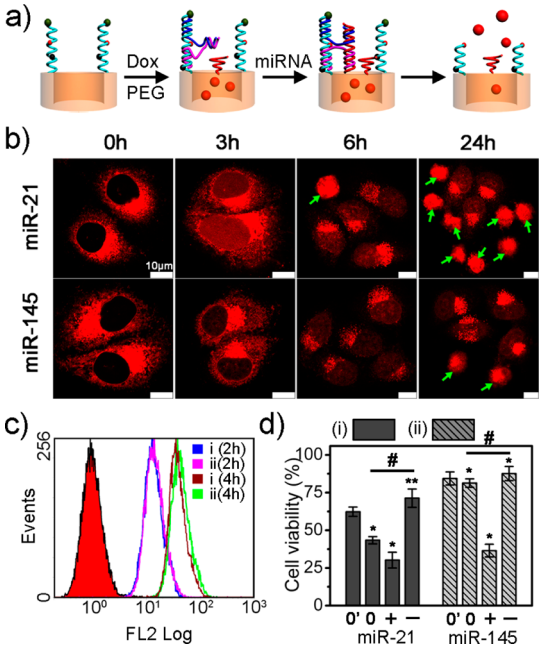

Figure 5. Intracellular delivery of MMSGRs-Dox-Apt/PEG nanocarriers and miRNA-triggered Dox release. (a) Illustration of the controlled Dox release from the nanocarriers by the cleavage of the substrates in the presence of miRNA. (b) CLSM images of HeLa cells after treatment of the nanocarriers respectively responsive to miR-21 and miR-145. After the cells were irradiated by NIR light for 30 min, the images were recorded as time went on. The apoptotic bodies of cells are marked with green arrows, which can be easily recognized in the merged confocal images in Supporting Information Figure S15. (c) Uptake amounts of (i) nanocarrier-21 and (ii) nanocarrier-145 by HeLa cells analyzed by flow cytometry. (d) Cytotoxicity of (i) nanocarrier-21 and (ii) nanocarrier-145 to HeLa cells after 24 h. The miRNA expression levels in HeLa cells were modulated without (0′ and 0) or with the transfection of the miRNA mimics (+) or inhibitors (−) for 6 h, and then all four groups were incubated with cultured medium containing respective nanocarriers for 6 h. After the replacement with fresh medium, the cells labeled with # were exposed under NIR light with a power density of 1.0 W cm^{-2} optimized in Supporting Information Figure S18 for 30 min; the cells treated without NIR exposure were set as control group (0′). Error bars indicate SD (n = 3). *p < 0.05, **p < 0.01 (two-tailed Student's t-test).

the introduction of miRNAs drastically accelerated the cleavage reaction and resulted in an intensified cytotoxicity, particularly under gentle NIR light exposure. Conversely, as shown in the PCR results (Supporting Information Figure S19), the transfection of inhibitor strands obviously reduced the miR-21 concentration and efficiently blocked the drug release, leading to high cell viability. Thus, the modulation of miRNA expression and NIR-irradiation power could act as a powerful tool to spatially and temporally control the drug release rates. Additionally, the nanocarriers exhibited excellent stability in cultured medium against nonspecific adsorption, acid degradation, and enzyme digestion (Supporting Information Figure S20). Therefore, with the screening of a more specific miRNA candidate as a therapeutic target, the versatile combination strategy was fully capable of achieving targeted delivery,

gene regulation, and controlled drug release *in vitro* or *in vivo*.

CONCLUSIONS

We have selected the deregulated miRNAs in cancer cells as model biomarkers and therapeutic targets to develop programmable nanodevices for logic operation, intracellular imaging, and controlled drug release. With the significant amplification of MNAzyme, the turn-on nanodevices presented high specificity and sensitivity in *in situ* detecting trace amounts of miRNAs in single cells, implying promising applications in accurate classification of cancer subtypes, dynamic monitoring of therapy response, and prognostic evaluation. More interestingly, miRNAs and their multiple target mRNAs constitute a complicated gene network to regulate different cellular pathways and processes. Not only can miRNAs be modulated by the transfection of their mimics or inhibitor to sensitize the tumor cells to drug response, for instance, the inhibition of miR-21 enhancing gemcitabine-induced apoptosis,[39] but in turn, the drug treatment also changes the miRNA expression levels such as the increased expression of miR-145 in Dox induction of p53.[40] Therefore, we have explored the construction of programmable nanocarriers to combine chemotherapy with gene therapy by modulating the expression of the target miRNAs for spatial-temporally controlling drug release and genetically alleviating drug resistance simultaneously, which paves a promising way for personalized treatment of human diseases. Finally, we emphasize that the efficacy of our multifunctional nanodevices in clinical cancer diagnosis and therapy was highly dependent on the reliability and specificity of the miRNA markers, indicating an urgent need to develop novel miRNA screening techniques, clarify the multiple role of miRNAs in disease, and improve the DNA synthesis and modification techniques by multidisciplinary cooperation at the nexus of chemistry, molecular biology, cell biology, and clinical medicine.

MATERIALS AND METHODS

Materials. All chemicals were listed in Supporting Information and used as received. Tris-HCl (20 mM, pH = 7.6) containing 146.0 mM NaCl, 5.0 mM KCl, and 5.0 mM $MgCl_2$ was used in cleavage reactions. All aqueous solutions were prepared using DEPC (diethylpyrocarbonate)-treated ultrapure water from a Milli-Q system. The substrate DNA sequences (sub-DNA) containing RNA nucleotides were purchased from Takara Biotechnology Co. Ltd. (Dalian, China). Other DNA oligonucleotide sequences were purchased from Shanghai Sangon Biological Engineering Technology & Services Co. (Shanghai, China). The microRNA sequences were obtained from Shanghai GenePharma (Shanghai, China).

Preparation of MMSGR Nanoprobes for miRNA Detection and MMSGRs-Dox-Apt/PEG Nanocarriers for miRNA-Triggered Drug Release. The GRs were prepared by a seed-mediated method with their concentration quantified as 25 nM by using optical extinction spectra.[41,42] With GRs as seed, the amine- and chloro-functionalized MSGRs were synthesized by a one-step method. Then MSGRs were reacted with a saturated solution of sodium azide in 20 mL of DMF at 90 °C for 12 h for azide functionalization. The resulting N_3-MSGRs were dispersed in methanol and refluxed for 24 h to remove cetyltrimethylammonium bromide (CTAB) and subsequently conjugated with alkynyl-modified sub-DNA *via* the click reaction of copper-catalyzed azide−alkyne cycloaddition (CuAAC) to obtain a 1.2 nM solution of sub-MSGRs. The sub-MSGRs were incubated with partzyme A and partzyme B to yield MMSGRs. By monitoring the UV−vis spectra of the DNA in the supernatant and in the stock solutions, the surface densities of the conjugated DNA on the MMSGRs were calculated. In a general experiment of miRNA detection, probe-21 was dispersed in 20 mM Tris-HCl buffer containing Mg^{2+}. The detection was initiated by the addition of miR-21 solutions with different concentrations under NIR irradiation. Changes in fluorescence due to cleavage of the sub-DNA-21 at the ribonucleotide were recorded at 520 nm with excitation at 485 nm at different times. Meanwhile, MMSGRs-Dox-Apt/PEG nanocarriers were prepared as follows. The sub-MSGRs were incubated with the Dox solution for 12 h, followed with the addition of partzymes A and B. After shaking the solution for another 12 h, the DNA aptamer AS1411-21 was added to hybridize with the remaining substrates on the surface of the MMSGRs. Finally, mPEG-SPA stock solution was added into the mixture for PEGylation to yield MMSGRs-Dox-Apt/PEG nanocarriers with a concentration of 1.2 nM. The Dox release experiments of MMSGRs-Dox-Apt/PEG were performed in 10 mM PBS containing 1 mM Mg^{2+}. After the addition of different concentrations of the miR-21 stock solutions, the Dox released from the nanocarriers was collected by centrifugation and measured by fluorescence spectrophotometry.

Polyacrylamide Gel Electrophoresis Analysis. Polyacrylamide gel (12%) was employed to verify the cleavage reaction in the absence and presence of miR-21. First, 10 μL of partzyme A-21 (1 μM) and 10 μL of partzyme B-21 (1 μM) were incubated with 10 μL of sub-DNA-21 (1 μM) in binding buffer at 37 °C for 3 h to form the stable DNA hybrid by partial paring hybridization at the end of each strand. Afterward, 10 μL of miR-21 (10 nM) was added and reacted at 50 °C for 0.5, 1, and 1.5 h. Electrophoresis was carried out at 100 V for 1 h at room temperature. After separation, the gel was stained with ethidium bromide and imaged by a fluorescence gel imaging system.

miRNA Detection by qRT-PCR. Cell transfection was performed following a standard protocol using Lipofectamine 2000 (Invitrogen, USA).[14] HeLa cells were cultured in FBS-free DMEM medium in a six-well plate with 50−70% confluence. Then miRNAs (5 μL, 100 μM) or their inhibitor strands (5 μL, 100 μM) were diluted into 250 μL of Opti-MEM medium to obtain solution A, while 7.5 μL of Lipofectamine 2000 was diluted into another 250 μL of Opti-MEM medium to obtain solution B. Solutions A and B were mixed and incubated for 20 min at room temperature, and then the complex was used to incubate the cells for 6 h at 37 °C. In the case of drug treatment, HL-60 cells were incubated with TPA for 24 h at a final concentration of 0, 10, and 100 nM. Finally, the total cellular RNAs were extracted from the cells using Trizol reagent (Invitrogen, USA) according to the manufacturer's protocols. The first-strand cDNA was generated using AMV reverse transcriptase (Takara Bio, Shiga, Japan) and a stem-loop RT primer (Invitrogen). Quantitative PCR was done with an ABI 7300 Sequence Detection System (Applied Biosystems) using SYBR Green PCR Master Mix. The relative expression of miRNA was calculated using the $2^{-\Delta CT}$ method, in which $\Delta CT = CT_{miRNA} - CT_{U6}$. All qRT-PCR reactions were performed in triplicate. miRNA detection was done by qRT-PCR. For analysis of the miR-21 level, we used 5′-ACA CTC CAG CTG GGT AGC TTA TCA GAC TGA-3′ as the forward primer and 5′-CTC AAC TGG TGT CGT GGA GTC GGC AAT TCA GTT GAG TCA ACA TC-3′ as the reverse primer, as well as 5′-CTC GCT TCG GCA GCA CA-3′ and 5′-AAC GCT TCA CGA ATT TGC GT-3′ for U6. The relative expression of miR-21 was calculated using the $2^{-\Delta CT}$

method, in which $\Delta CT = CT_{miR\text{-}21} - CT_{U6}$. All qRT-PCR reactions were performed in triplicate. In the case of detecting miR-145, 5′-ACA CTC CAG CTG GGG TCC AGT TTT CCC AGG A-3′ was used as the forward primer, and 5′-CTC AAC TGG TGT CGT GGA GTC GGC AAT TCA GTT GAG AGG GAT TC-3′ was used as the reverse primer.

Cell Culture. HeLa, NIH 3T3, and HL-60 were obtained from the Institute of Cell Biology at the Chinese Academy of Sciences (Shanghai, P. R. China) and cultured in DMEM (Life Technologies, Grand Island, NY, USA) at 37 °C under 5% CO_2 atmosphere, supplemented with L-glutamine (2 mM) and 10% fetal bovine serum (FBS). At the logarithmic growth phase, the cells were incubated with different nanodevices in cultured medium.

Intracellular miRNA Imaging and Controlled Dox Release. The general detection of intracellular miRNA with MMSGRs probes was performed as follows: the cells were treated with the probes for 6 h, then washed with PBS and cultured with fresh medium upon irradiation with NIR light for 30 min at different power densities. The fluorescence signals were recorded by flow cytometry or CLSM. In the controlled drug release triggered by intracellular miRNA, the cells were generally treated with the MMSGRs-Dox-Apt/PEG nanocarriers for 6 h. The cells were washed with PBS three times and irradiated with NIR light at different power densities for 30 min. To minimize the damage to the cells caused by NIR irradiation, all the NIR irradiation was performed as follows: the cells were exposed to NIR light for 30 s and the NIR light was removed for 30 s; then the procedure was repeated in 30 min. The amounts of the nanocarriers internalized into the cells were evaluated by flow cytometry, while the drug release inside HeLa cells was monitored by CLSM. The therapeutic efficiency of the nanocarriers was assessed through cell viability by the MTT (3-(4,5-dimethylthiazol-2-yl)-2,5-diphenyltetrazolium bromide) assay. Briefly, the cells were cultured in a 96-well plate at a density of 10 000 cells in each well. After treatment with the nanocarriers for the indicated time, the medium was removed, and fresh medium (100 μL) containing MTT (20 μL, 5 mg mL^{-1}) was added into each well. After 4 h of incubation, the medium was replaced by DMSO and the absorbance of the solution was measured to assess the relative viability of the cells using a Bio-Rad 680 microplate reader. The optical density (OD) was read at a wavelength of 490 nm. Relative cell viability was expressed as ([OD]test/[OD]control) × 100%. Each experiment was repeated at least three times.

Conflict of Interest: The authors declare no competing financial interest.

Supporting Information Available: Chemicals, DNA and RNA sequences, detailed experimental procedures, characterization of the nanodevices, analysis of the nanoprobes in miRNA imaging, and evaluation of the specificity, efficiency, and stability of the drug nanocarriers. This material is available free of charge *via* the Internet at http://pubs.acs.org.

Acknowledgment. This research was supported by the National Basic Research Program of China (2011CB933502), National Natural Science Foundation of China (21335004, 21205060, 21427807), and the Program A for Outstanding PhD Candidate of Nanjing University.

REFERENCES AND NOTES

1. Calin, G. A.; Croce, C. M. MicroRNA Signatures in Human Cancers. *Nat. Rev. Cancer* **2006**, *6*, 857–866.
2. O'Connell, R. M.; Rao, D. S.; Chaudhuri, A. A.; Baltimore, D. Physiological and Pathological Roles for MicroRNAs in the Immune System. *Nat. Rev. Immunol.* **2010**, *10*, 111–122.
3. Di Leva, G.; Garofalo, M.; Croce, C. M. MicroRNAs in Cancer. *Annu. Rev. Pathol.: Mech. Dis.* **2014**, *9*, 287–314.
4. Lu, J.; Getz, G.; Miska, E. A.; Alvarez-Saavedra, E.; Lamb, J.; Peck, D.; Sweet-Cordero, A.; Ebert, B. L.; Mak, R. H.; Ferrando, A. A.; Downing, J. R.; Jacks, T.; Horvitz, H. R.; Golub, T. R. MicroRNA Expression Profiles Classify Human Cancers. *Nature* **2005**, *435*, 834–838.
5. Yu, Z.; Baserga, R.; Chen, L.; Wang, C.; Lisanti, M. P.; Pestell, R. G. MicroRNA, Cell Cycle, and Human Breast Cancer. *Am. J. Pathol.* **2010**, *176*, 1058–1064.
6. Iorio, M. V.; Casalini, P.; Tagliabue, E.; Menard, S.; Croce, C. M. MicroRNA Profiling as a Tool to Understand Prognosis, Therapy Response and Resistance in Breast Cancer. *Eur. J. Cancer* **2008**, *44*, 2753–2759.
7. Pritchard, C. C.; Cheng, H. H.; Tewari, M. MicroRNA Profiling: Approaches and Considerations. *Nat. Rev. Genet.* **2012**, *13*, 358–369.
8. Dong, H.; Lei, J.; Ding, L.; Wen, Y.; Ju, H.; Zhang, X. MicroRNA: Function, Detection, and Bioanalysis. *Chem. Rev.* **2013**, *113*, 6207–6233.
9. Lu, J.; Tsourkas, A. Imaging Individual MicroRNAs in Single Mammalian Cells *in Situ*. *Nucleic Acids Res.* **2009**, *37*.
10. Deng, R.; Tang, L.; Tian, Q.; Wang, Y.; Lin, L.; Li, J. Toehold-Initiated Rolling Circle Amplification for Visualizing Individual MicroRNAs *in Situ* in Single Cells. *Angew. Chem., Int. Ed.* **2014**, *53*, 2389–2393.
11. De Planell-Saguer, M.; Rodicio, M. C.; Mourelatos, Z. Rapid *in Situ* Codetection of Noncoding RNAs and Proteins in Cells and Formalin-Fixed Paraffin-Embedded Tissue Sections without Protease Treatment. *Nat. Protocols* **2010**, *5*, 1061–1073.
12. Ge, J.; Zhang, L. L.; Liu, S. J.; Yu, R. Q.; Chu, X. A Highly Sensitive Target-Primed Rolling Circle Amplification (TPRCA) Method for Fluorescent *in Situ* Hybridization Detection of MicroRNA in Tumor Cells. *Anal. Chem.* **2014**, *86*, 1808–1815.
13. Andorfer, C. A.; Necela, B. M.; Thompson, E. A.; Perez, E. A. MicroRNA Signatures: Clinical Biomarkers for the Diagnosis and Treatment of Breast Cancer. *Trends Mol. Med.* **2011**, *17*, 313–319.
14. Zhang, P.; Cheng, F.; Zhou, R.; Cao, J.; Li, J.; Burda, C.; Min, Q.; Zhu, J.-J. DNA-Hybrid-Gated Multifunctional Mesoporous Silica Nanocarriers for Dual-Targeted and MicroRNA-Responsive Controlled Drug Delivery. *Angew. Chem., Int. Ed.* **2014**, *53*, 2371–2375.
15. Yang, P. P.; Gai, S. L.; Lin, J. Functionalized Mesoporous Silica Materials for Controlled Drug Delivery. *Chem. Soc. Rev.* **2012**, *41*, 3679–3698.
16. Nair, M.; Guduru, R.; Liang, P.; Hong, J.; Sagar, V.; Khizroev, S. Externally Controlled on-Demand Release of Anti-HIV Drug Using Magneto-Electric Nanoparticles as Carriers. *Nat. Commun.* **2013**, *4*, 1707.
17. Zhang, J.; Yuan, Z. F.; Wang, Y.; Chen, W. H.; Luo, G. F.; Cheng, S. X.; Zhuo, R. X.; Zhang, X. Z. Multifunctional Envelope-Type Mesoporous Silica Nanoparticles for Tumor-Triggered Targeting Drug Delivery. *J. Am. Chem. Soc.* **2013**, *135*, 5068–5073.
18. Bartel, D. P. MicroRNAs: Genomics, Biogenesis, Mechanism, and Function. *Cell* **2004**, *116*, 281–297.
19. Zhang, P.; Zhang, J.; Wang, C.; Liu, C.; Wang, H.; Li, Z. Highly Sensitive and Specific Multiplexed MicroRNA Quantification Using Size-Coded Ligation Chain Reaction. *Anal. Chem.* **2013**, *86*, 1076–1082.
20. Wang, X. P.; Yin, B. C.; Wang, P.; Ye, B. C. Highly Sensitive Detection of MicroRNAs Based on Isothermal Exponential Amplification-Assisted Generation of Catalytic G-Quadruplex DNAzyme. *Biosens. Bioelectron.* **2013**, *42*, 131–135.
21. Liu, X.; Niazov-Elkan, A.; Wang, F.; Willner, I. Switching Photonic and Electrochemical Functions of a DNAzyme by DNA Machines. *Nano Lett.* **2013**, *13*, 219–25.
22. Ali, M. M.; Aguirre, S. D.; Lazim, H.; Li, Y. Fluorogenic DNAzyme Probes as Bacterial Indicators. *Angew. Chem., Int. Ed.* **2011**, *50*, 3751–3754.
23. Hollenstein, M.; Hipolito, C.; Lam, C.; Dietrich, D.; Perrin, D. M. A Highly Selective DNAzyme Sensor for Mercuric Ions. *Angew. Chem., Int. Ed.* **2008**, *47*, 4346–4350.
24. Wu, P.; Hwang, K.; Lan, T.; Lu, Y. A DNAzyme-Gold Nanoparticle Probe for Uranyl Ion in Living Cells. *J. Am. Chem. Soc.* **2013**, *135*, 5254–5257.
25. Kuo, T.-R.; Hovhannisyan, V. A.; Chao, Y.-C.; Chao, S.-L.; Chiang, S.-J.; Lin, S.-J.; Dong, C.-Y.; Chen, C.-C. Multiple Release Kinetics of Targeted Drug from Gold Nanorod

Embedded Polyelectrolyte Conjugates Induced by Near-Infrared Laser Irradiation. *J. Am. Chem. Soc.* **2010**, *132*, 14163–14171.
26. Liang, L.; Astruc, D. The Copper(I)-Catalyzed Alkyne-Azide Cycloaddition (CuAAC) "Click" Reaction and Its Applications. An Overview. *Coord. Chem. Rev.* **2011**, *255*, 2933–2945.
27. Krichevsky, A. M.; Gabriely, G. miR-21: a Small Multi-Faceted RNA. *J. Cell. Mol. Med.* **2009**, *13*, 39–53.
28. Li, S.; Liang, Z.; Xu, L.; Zou, F. MicroRNA-21: A Ubiquitously Expressed Pro-survival Factor in Cancer and Other Diseases. *Mol. Cell. Biochem.* **2012**, *360*, 147–158.
29. Kitade, Y.; Akao, Y. MicroRNAs and Their Therapeutic Potential for Human Diseases: microRNAs, miR-143 and -145, Function as Anti-Oncomirs and the Application of Chemically Modified miR-143 as an Anti-Cancer Drug. *J. Pharmacol. Sci.* **2010**, *114*, 276–280.
30. Jansson, M. D.; Lund, A. H. MicroRNA and Cancer. *Mol. Oncol.* **2012**, *6*, 590–610.
31. Neilson, J. R.; Zheng, G. X. Y.; Burge, C. B.; Sharp, P. A. Dynamic Regulation of MiRNA Expression in Ordered Stages of Cellular Development. *Genes Dev.* **2007**, *21*, 578–589.
32. Slowing, I.; Trewyn, B. G.; Lin, V. S. Y. Effect of Surface Functionalization of MCM-41-Type Mesoporous Silica Nanoparticles on the Endocytosis by Human Cancer Cells. *J. Am. Chem. Soc.* **2006**, *128*, 14792–14793.
33. Asefa, T.; Tao, Z. M. Biocompatibility of Mesoporous Silica Nanoparticles. *Chem. Res. Toxicol.* **2012**, *25*, 2265–2284.
34. Kasashima, K.; Nakamura, Y.; Kozu, T. Altered Expression Profiles of MicroRNAs during TPA-Induced Differentiation of HL-60 Cells. *Biochem. Biophys. Res. Commun.* **2004**, *322*, 403–410.
35. Zhang, Z.; Balogh, D.; Wang, F.; Willner, I. Smart Mesoporous SiO_2 Nanoparticles for the DNAzyme-Induced Multiplexed Release of Substrates. *J. Am. Chem. Soc.* **2013**, *135*, 1934–1940.
36. Chen, C.; Geng, J.; Pu, F.; Yang, X. J.; Ren, J. S.; Qu, X. G. Polyvalent Nucleic Acid/Mesoporous Silica Nanoparticle Conjugates: Dual Stimuli-Responsive Vehicles for Intracellular Drug Delivery. *Angew. Chem., Int. Ed.* **2011**, *50*, 882–886.
37. Chen, C.; Pu, F.; Huang, Z.; Liu, Z.; Ren, J.; Qu, X. Stimuli-Responsive Controlled-Release System Using Quadruplex DNA-Capped Silica Nanocontainers. *Nucleic Acids Res.* **2011**, *39*, 1638–1644.
38. Zhang, Y. F.; Yuan, Q.; Chen, T.; Zhang, X. B.; Chen, Y.; Tan, W. H. DNA-Capped Mesoporous Silica Nanoparticles as an Ion-Responsive Release System to Determine the Presence of Mercury in Aqueous Solutions. *Anal. Chem.* **2012**, *84*, 1956–1962.
39. Meng, F.; Henson, R.; Lang, M.; Wehbe, H.; Maheshwari, S.; Mendell, J. T.; Jiang, J.; Schmittgen, T. D.; Patel, T. Involvement of Human Micro-RNA in Growth and Response to Chemotherapy in Human Cholangiocarcinoma Cell Lines. *Gastroenterology* **2006**, *130*, 2113–2129.
40. Suzuki, H. I.; Yamagata, K.; Sugimoto, K.; Iwamoto, T.; Kato, S.; Miyazono, K. Modulation of MicroRNA Processing by p53. *Nature* **2009**, *460*, 529–533.
41. Ye, X.; Jin, L.; Caglayan, H.; Chen, J.; Xing, G.; Zheng, C.; Doan-Nguyen, V.; Kang, Y.; Engheta, N.; Kagan, C. R.; Murray, C. B. Improved Size-Tunable Synthesis of Monodisperse Gold Nanorods through the Use of Aromatic Additives. *ACS Nano* **2012**, *6*, 2804–2817.
42. Orendorff, C. J.; Murphy, C. J. Quantitation of Metal Content in the Silver-Assisted Growth of Gold Nanorods. *J. Phys. Chem. B* **2006**, *110*, 3990–3994.